Monte Carlo studies on geometrically confined skyrmions in nanodots: Stability and morphology under radial stresses

G. Diguet, Benjamin Ducharne, S. El Hog, F. Kato, H. Koibuchi, T. Uchimoto, H.T. Diep

Monte Carlo Studies on Geometrically Confined Skyrmions in Nanodots: Stability and Morphology under Radial Stresses

G. Diguet*

Micro System Integration Center, Tohoku University, Sendai, Japan

B. Ducharne

INSA Lyon, Universite de Lyon, Villeurbanne Cedex, France and

ElyTMax, CNRS-Universite de Lyon-Tohoku University, Sendai, Japan

S. El Hog

Université de Monastir (LMCN), Monastir, Tunisie

F. Kato and H. Koibuchi†

National Institute of Technology (KOSEN),

Ibaraki College, Hitachinaka, Japan.

T. Uchimoto

Institute of Fluid Science (IFS), Tohoku University, Sendai, Japan and

ELyTMaX, CNRS-Universite de Lyon-Tohoku University, Sendai, Japan

H. T. Diep‡

CY Cergy Paris University, Cergy-Pontoise, France

Abstract

We numerically study the stability and morphology of geometrically confined skyrmions (skys) in nanodots, which have been experimentally observed and reported, using the Finsler geometry modeling technique, which dynamically implements anisotropies in ferromagnetic interaction, Dzyaloshinskii-Moriya interaction, and magneto-elastic coupling in response to mechanical stresses. We find a geometric confinement (GC) effect that stabilizes skys in small-diameter nanodots under a low external magnetic field. We also find a strain effect that stabilizes a single sky at the center of the nanodots without a magnetic field. Moreover, we find that the obtained Monte Carlo data on the morphological changes between the two different phases of sky and stripe are consistent with the reported experimental data obtained by Wang et al. The numerical results indicate that the dynamical anisotropy of the coupling constants originating from radial tensile stresses and the GC effect suitably explain the sky stability on nanodots without a magnetic field.

* gildas.diguet.d4@tohoku.ac.jp

† koi-hiro@sendai-nct.ac.jp; koibuchih@gmail.com

‡ diep@cyu.fr

I. INTRODUCTION

A topologically stable spin configuration called skyrmion (sky) emerges in chiral magnetic materials under competition between ferromagnetic interaction (FMI) and Dzyaloshinskii-Moriya interaction (DMI), and many studies have been conducted [1–7] since its experimental discovery [8–10]. It is well known that skys are stabilized by an external magnetic field via Zeeman energy and mechanical strains via magnetoelastic coupling (MEC) and magnetic anisotropy [11, 12]. The confinement of skys in small domains, called geometric confinement (GC), has also been proposed as a stabilization technique [13], and several experimental and numerical studies on GC and strain effects have been conducted [14–21].

Wang et al. demonstrated the application of the GC of skys to electric switching, including the emergence of the sky without a magnetic field on nanodots with a diameter of 350 nm, in combination with GC and strain effects [20]. They reported experimental data on the underlying GC effects without strain as well as morphological changes in spin configurations under radial stress. Their results show that the strain effects on magnetic anisotropy and DMI are crucial for morphological changes and sky manipulation on nanodots, and their statement indicates that sky formation by an external magnetic field is different from that by radial stress. The stabilization of the sky on nanodots without an external magnetic field was numerically confirmed under a specific boundary condition [21], and the effects of magnetic anisotropy were studied numerically [22]. A GC effect for stabilizing sky vortex was also observed in tetrahedral nanoparticles [23]. Based on these studies, the effects of GC, role of strains, and interaction anisotropies on these morphological changes and sky formation have been clarified. However, the origins of these effects remain unclear.

In this study, we apply Finsler geometry (FG) modeling to clarify the effects of GC and strain on experimentally observed morphological changes in spin configurations in nanodots using the Monte Carlo (MC) simulation technique [24]. Dynamical anisotropies in the FMI, DMI, and MEC that emerged under radial stresses are numerically evaluated to explain the sky stability in nanodots. FG modeling can implement anisotropic effects on interactions simply caused by distance anisotropy. Distance anisotropy is dynamically changeable because it is implemented by internal degrees of freedom, such as the strain direction, which can be controlled by direction-dependent external stimuli, such as radial stresses. For this simple geometric treatment of interactions, FG modeling allows us to perform theoretical

studies on skys based on the same input-output relation as experimental studies. This is the main advantage of FG modeling over standard modeling, in which anisotropic interactions are implemented using manually fixed strains and anisotropic interaction coefficients.

II. MODEL HAMILTONIAN AND 3D CYLINDRICAL LATTICES

A. 3D cylindrical lattices and radial stresses

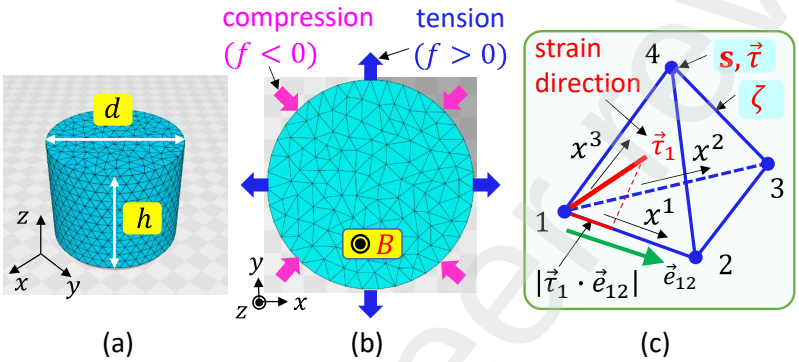

FIG. 1. (a) A cylindrical lattice of radius d and height h, (b) illustrations of tensile ($f>0$) and compressive ($f<0$) stresses radially applied to cylindrical lattice, (c) strain direction $\vec{\tau}_1$ at vertex 1 and its component $|\vec{\tau}_1 \cdot \vec{e}_{12}|$, where $\|\vec{e}_{12}\|=1$, along a local coordinate axis x^1 of a tetrahedron with vertices 1, 2, 3 and 4. The variables $\mathbf{s}, \vec{\tau}$ are defined at vertices and ζ on bonds.

Cylindrical lattices constructed using the Voronoi tesselation technique [25] are used to simulate skys on nanodots [20] (Fig. 1(a)). The total number of vertices is $N=2083$, 5430, 8465, and $N=11962$, and the ratio $R=d/h$ of diameter d and a fixed height $h=12a$ is given by $R=1.2a$, $2a$, $2.5a$, and $R=3a$ in the unit of $a(=\sqrt{3}/2)$ (see Appendix A for further details on the lattice structure). Mechanical stresses $f>0$ and $f<0$ are applied along the radial direction and a magnetic field B is applied along the z direction (Fig. 1(b)). The directions of magnetic field and stresses are the same as those in [20].

B. Hamiltonian and Monte Carlo

We use the following discrete Hamiltonian:

$$H(\mathbf{s},\vec{\tau},\zeta) = \lambda H_{\rm FM} + D H_{\rm DM} + H_B + \alpha H_{\rm ME} + H_f + \delta H_\zeta, \tag{1}$$

where $\mathbf{s}(\in S^2$: unit sphere) and $\vec{\tau}(\in S^2/2$: half sphere) denote the spin and strain variables, respectively, defined at every lattice vertex, and $\zeta(\in \{1,-1\})$ on the bonds (Fig. 1(c)); ζ is a variable to implement a dynamical anisotropy in MEC. A free boundary condition is assumed for variables on the surface. The symbols $\lambda, D, \alpha, \delta$ on the right-hand side represent the interaction coefficients. The first three terms in Eq. (1) describe the FMI, DMI, and Zeeman energies; the next two terms are the magneto-elastic coupling energy $H_{\rm ME}$ and mechanical energy H_f, and the final term H_ζ, which is not included in the model of Ref. [24], describes a dynamical Finsler length for an anisotropic MEC in $H_{\rm ME}$ (Appendix B for further details on the discrete Hamiltonian). In the case of a zero stress, $f=0$ or equivalently $\alpha=0$, the spin configurations are determined only by the first three terms. For this reason, no spontaneous magnetic anisotropy is assumed in the model; therefore, the target material in the present paper is not exactly the same as that experimentally studied in Ref. [20]. Additionally, the materials used in Ref. [20] are layered ones and a Neel-type sky is assumed in their simulations; in contrast, the materials in the present paper are single-layer and not always thin, in which a Bloch-type sky is assumed.

The partition function is given by

$$Z = \sum_{\mathbf{s}} \sum_{\vec{\tau}} \sum_{\zeta} \exp\left[-H(\mathbf{s}, \vec{\tau}, \zeta)/T\right], \tag{2}$$

where T is the temperature and $\sum_{s,\tau,\zeta}$ denotes the sum over all possible configurations of $\mathbf{s}, \vec{\tau}$ and ζ. The mean value of physical quantity P_q is defined by the ensemble average $\langle P_q \rangle = \sum_{s,\tau,\zeta} P_q \exp(-H/T)/Z$, which is calculated by Metropolis MC technique [26, 27] using the sample average $\langle P_q \rangle = \sum_i P_q(i) / \sum_i 1$, where $P_q(i)$ is i-th sample evaluated by the lattice average. N consecutive updates for each of the three variables are examined, and a uniform random number is used to select N from N_B ζ-variables defined on the bonds, where N_B is the total number of bonds (Appendix A). A new variable $\mathbf{s}'$ is randomly generated, independent of the present $\mathbf{s}$ and updated with probability $\mathrm{Min}[1, \exp -(H_{\rm new} - H_{\rm old})]$. The same procedure is applied to the variable $\vec{\tau}$. In the update of $\zeta(\in\{-1,1\})$, we fix ζ' to the opposite to the present ζ and accept ζ' with the same procedure.

The total number of MC sweeps (MCSc) for the calculation of physical quantities is 5.25×10^7. The samples are calculated at every 500 MCSs after $7.5\times10^6 \sim 12.5\times10^6$ MCSs for thermalization starting with random initial configurations of the variables.

III. RESULTS

A. Size effect

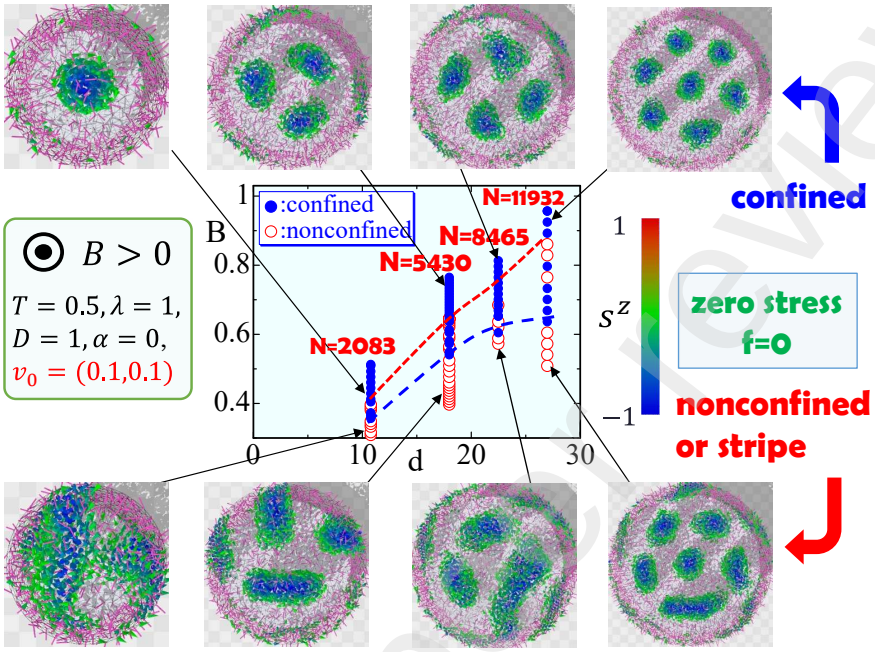

FIG. 2. Phase diagram of B vs. d for confined sky (•) and nonconfined or stripe (○) observed on four different lattices, where d is the diameter of lattice in the unit of the edge length (= 1) of a regular triangle (Appendix A). Spins of $s^z < 0$ are plotted with small cones in the snapshots.

First, we demonstrate a size effect that enables the sky to emerge with a small external magnetic field on the smaller nanodots. The assumed parameters are shown in Fig. 2; $v_0 = (0.1, 0.1)$ denotes that $v_0 = 0.1$ for both the FMI and DMI in Eq. (C1). v_0 plays a role in the strength of anisotropy; however, it does not play any role in anisotropy of interactions in the case of $f = 0$, where $\vec{\tau}$ is isotropic. Plots in Fig. 2 represent configurations of confined sky (•) and nonconfined or stripe (○) observed on four different lattices (Appendix A). The color code represents s^z, and the spins of $s^z < 0$ are plotted with cones, and small cylinders or lines represent the direction of $\vec{\tau}$. All the plotted data are obtained by visually evaluating whether the skys are confined using the snapshots. The dashed line in red (blue) shows the upper (lower) limit of B for the nonconfined (confined) phase. The region between these two dashed lines is similar to the range of two-phase coexistence; however, it does not always imply a first-order phase transition because no clear jump is observed in physical

quantities, including the topological charge between the confined sky and non-confined sky phases. Interestingly, the result that the two-phase coexistence region of B decreases as d decreases is qualitatively consistent with the experimental data reported in Ref. [20].

Notably, the confinement mechanism in the model originates from a surface effect, in which the absolute value of the surface DMI coefficient is smaller than that of the bulk DMI [28]. A static part of this difference in the DMI strength between the surface and bulk for $f = 0$ and a dynamical enhancement of the difference for $f > 0$ are intuitively understood from the discrete form of H_{DM} in Eq. (B2) (see Appendix C).

B. Strain effect

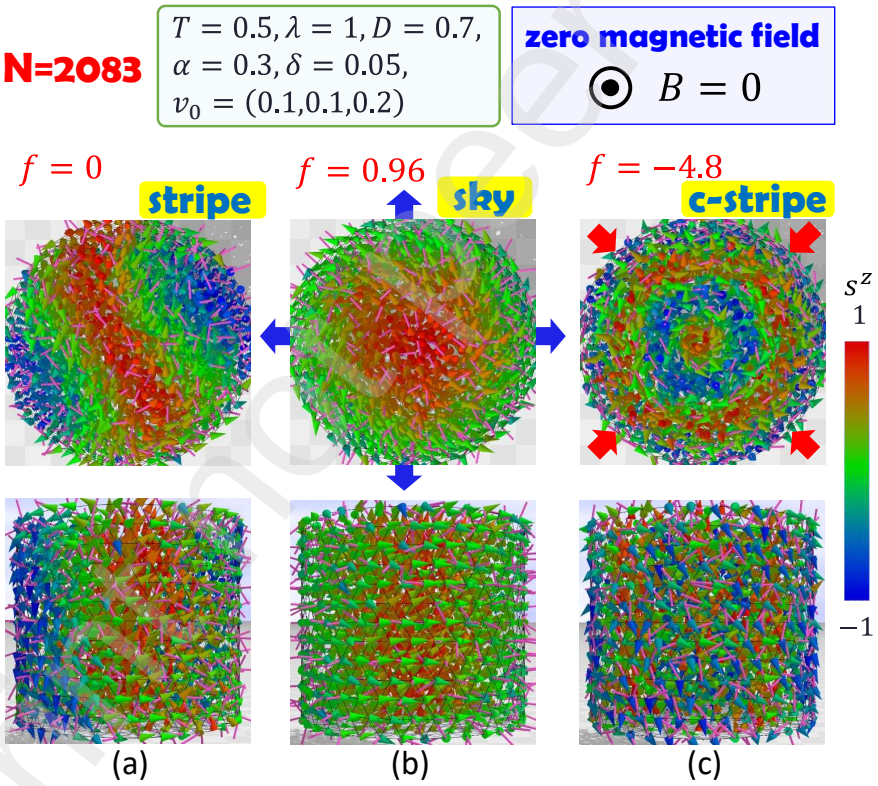

FIG. 3. Snapshots obtained for (a) $f = 0$, (b) $f = 0.96$ (tension), and (c) $f = -4.8$ (compression) on the $N = 2083$ lattice. We find stripe, sky, and c-stripe (circular stripe) phases for zero, positive, and negative stresses, consistent with the reported experimental data for thick-layered case [20].

Next, we show the effects of the strain caused by radial tension ($f > 0$) and compression ($f < 0$) under a zero external magnetic field ($B = 0$). The assumed parameters are shown

in Fig. 3; $v_0 = (0.1, 0.1, 0.2)$ denotes that $v_0 = 0.1$ for both FMI and DMI in Eq. (C1) and $v_0 = 0.2$ for MEC in Eq. (C2), which are fixed in this study. The snapshots obtained for the $N = 2083$ lattice are shown in Figs. 3(a)–(c), where top and side views are plotted in (a) $f = 0$, (b) $f = 0.96$, and (c) $f = -4.8$. Small cylinders representing $\vec{\tau}$ can be viewed as (a) isotropic, (b) radially aligned, and (c) spiral along the z direction. These observations are consistent with expectations because $\vec{\tau}$ represents the elongation direction owing to the radial stress f. It should be noted that the spin direction at the center of the sky in Fig. 3(b) is spontaneously determined and opposite to that plotted in Fig. 2. This spontaneous direction occurs because $B = 0$, in contrast with the case in Ref. [20], where a small magnetic field is applied for atomic microscopy measurements, even with a zero external magnetic field. Note also that the radial stress, for example, compression, is well defined only in 3 dimensional models because of the induced deformation of the nanodots along the z direction indicated by the $\vec{\tau}$ direction.

The configuration in (c) is considered to be a circular stripe, which is different from "vortex" observed in Ref. [20] for the thin-layered case. However, in their experiment on the thick-layered case, stripes were observed, which are consistent with our numerical data in the sense that both are stripe, although our results correspond to "circular" stripes. We checked that these morphological changes under radial stresses can also be observed in the case of Neel type sky.

C. Order parameters

Now, we calculate nonpolar order parameters of spins

$$\begin{aligned} Q_s^\mu =& \frac{3}{2}\left(\langle(\mathbf{s}\cdot\vec{e}_i^{\,\mu})^2\rangle - \frac{1}{3}\right), \\ & (-0.5 \le Q_s^\mu \le 1), \quad (\mu = r, \theta, z), \\ Q_s^{\rm in} =& Q_s^r + Q_s^\theta, \end{aligned} \tag{3}$$

where $\vec{e}_i^{\,r}$ and $\vec{e}_i^{\,\theta}$ denote unit vectors along the radial and tangential directions at vertex i, respectively (Appendix D). Order parameters of this type are always used for liquid crystal molecules [29]. The results are shown in Fig. 4(a) with snapshots in Figs. 4(b)–(g). The parameters $Q_s^\mu(\mu = r, \theta, z)$ and $Q_s^{\rm in}$ indicate that the sky phase is separated from the stripe phase. We find an intermediate phase denoted by "r-stripe" (rounded stripe)

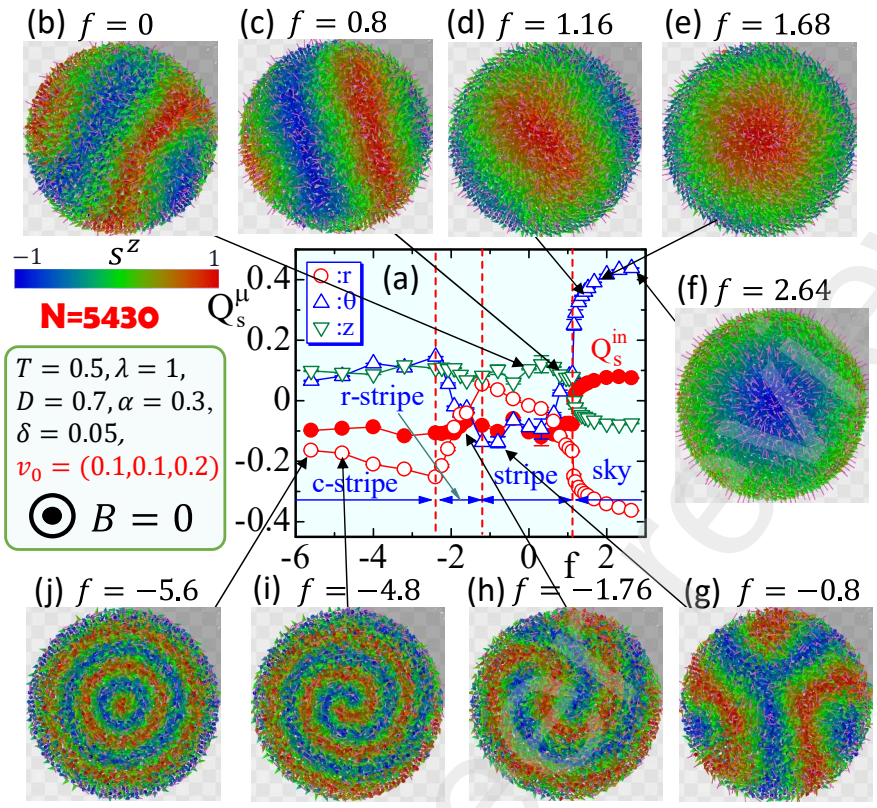

FIG. 4. (a) Nonpolar order parameters $Q_s^\mu (\mu = r, \theta, z)$ and $Q_s^{\rm in}$ vs. f, and (b)–(j) snapshots for $-5.6 \le f \le 2.64$ obtained on the $N = 5430$ lattice under $B = 0$. We find two different phases sky and stripe, and the stripe phase can be divided into three phases; stripe, "c-stripe" (circular stripe), and an intermediate phase "r-stripe" (rounded stripe) between the stripe and c-stripe phases. We find elongated sky in (d) and perfect sky in (e) and (f), in which the signs of s^z at the periphery are opposite to those at the center. (i) is a spiral stripe, which is also stable.

between circular stripe and stripe phases from Q_s^r and Q_s^θ. The sky and stripe phases are characterized by $Q_s^{\rm in}$ (•), though the difference of which is not so large.

Here, we discuss the difference in Q_s^r among the circular stripe, stripe, and sky phases. In the circular stripe phase (Figs. 4(i),(j)), $s^r \to 0$, and therefore, $\langle (\mathbf{s} \cdot \vec{e}_i^{\,r})^2 \rangle \to 0$ ($\Leftrightarrow Q_s^r \to -0.5$) is expected and confirmed in Fig. 4(a). In the stripe phase (Figs. 4(b),(c)), we find $Q_s^r \to 0$ implying $\langle (\mathbf{s} \cdot \vec{e}_i^{\,r})^2 \rangle \to 1/3$, which means that 1/3 of $\mathbf{s}$ align along the $\pm r$ direction. In the sky phase (Figs. 4(e),(f)), it is apparent that $\langle (\mathbf{s} \cdot \vec{e}_i^{\,r})^2 \rangle \to 0$ ($\Leftrightarrow Q_s^r \to -0.5$).

It should be noted that the total number of circular stripes of the $N = 5430$ lattice is larger than that of the $N = 2803$ lattice in Fig. 3 because the lattice diameter d approximately increases 1.7 times. Such a change in the number can also be observed in the stripe phase.

By contrast, the total number (=1) of skys in the sky phase remains unchanged and is independent of d, and the sky looks like a vortex [30, 31], in sharp contrast to the case of nonzero magnetic field with $f = 0$ in Fig. 2. This sky modification is expected to be owing to the strong MEC effect for a relatively large $f(> 0)$, where a strain configuration ($\Leftrightarrow \vec{\tau} \propto \vec{r}/r$) shares the center with the sky for the rotational symmetry independent of N (Fig. 4(f)). Owing to this symmetry, there is no chance for skys to appear independently of the primary sky on nanodots. In addition, this rotational symmetry is compatible with the surface effect, in which the DMI is small on the surface compared with the bulk DMI.

The sign of s^z at the periphery of skys emerged under the tensile stress is not always completely opposite to that at the center as shown in Figs. 4(d),(e) and (f). Therefore, these skys resemble vortex configurations, as mentioned above [30, 31]. However, the opposite sign of s^z at the periphery is apparent when f is not large such as $f = 1.68$ in Fig. 4(e), for example. Therefore, the configurations shown in Figs. 4(d),(e) and (f) are considered to be sky.

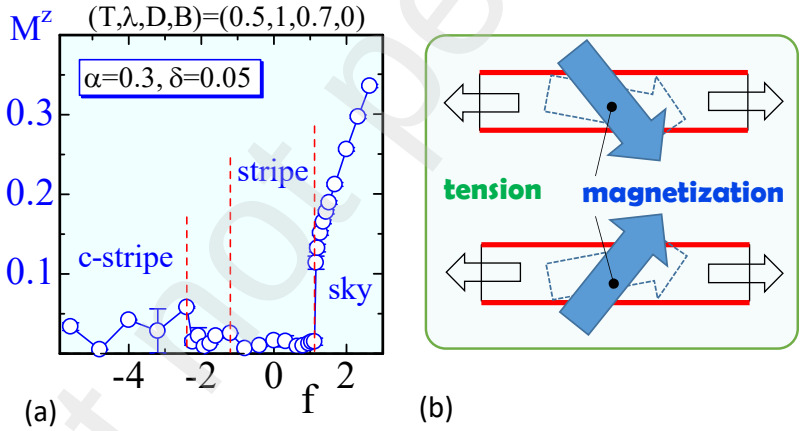

FIG. 5. (a) Polar order parameter M^z vs. f, and (b) an illustration of strain effects on magnetization in the case of tension.

To see effects of strains on magnetization, we plot the absolute of polar order parameters

$$M^z = \frac{1}{N} |\sum_i s_i^z|, \tag{4}$$

in Fig. 5(a), where the dashed vertical lines represent the phase boundaries plotted in Fig. 4(a). We find in the sky phase that M^z increases from $M^z = 0$ to $M^z > 0$ as f increases in the sky phase. The response of M^z is illustrated in Fig. 5(b), which is the same as that

observed as inverse magnetostriction. This behavior of M^z indicates that **s** at the central region of nanodots aligns along the $\pm z$ direction as f increases and that f effectively plays a role in "nonpolar" magnetic field along the z direction in the sky phase. $M^z \to 0$ in the stripe phases because **s** that align along the $\pm z$ directions cancel with each other.

D. Direction-dependent interaction coefficients with effective Hamiltonians and topological charge

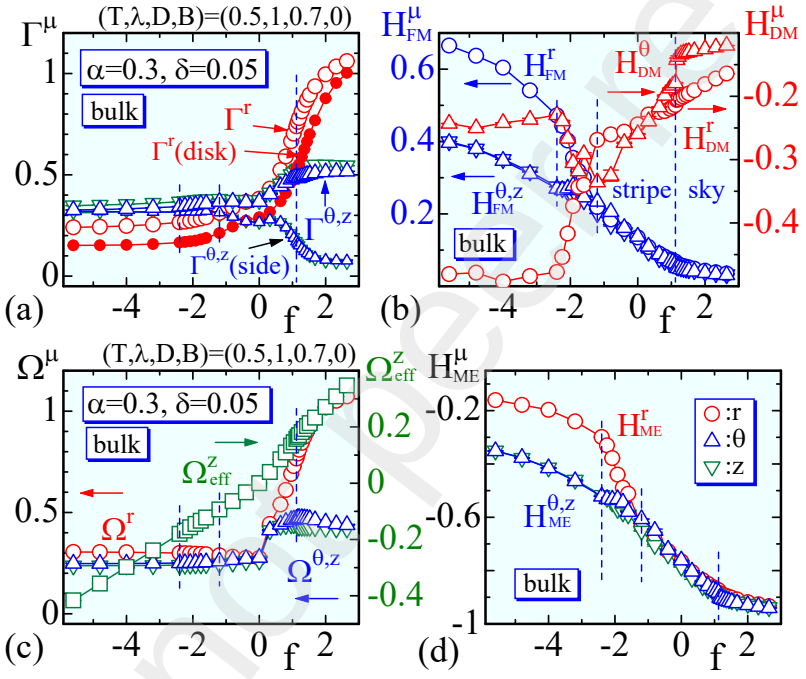

FIG. 6. (a) Direction-dependent coefficients $\Gamma^\mu = \langle \Gamma^\mu_{ij} \rangle, (\mu = r, \theta, z)$ vs. f, where $\Gamma^{\theta,z}$(side) and Γ^r(disk) denote the θ, z components on the side surface and the r component on the upper and lower disks, and (b) the corresponding bulk Hamiltonian $H^\mu_{\rm FM}$ and $H^\mu_{\rm DM}$ (Appendix D). (c) The coefficient of the magneto-elastic coupling $\Omega^\mu = \langle \Omega^\mu_{ij} \rangle$, and (d) the corresponding Hamiltonian $H^\mu_{\rm ME}$.

The direction-dependent coefficients $\Gamma^\mu = \langle \Gamma^\mu_{ij} \rangle, (\mu = r, \theta, z)$ and the corresponding $H^\mu_{\rm FM,DM}$ are calculated using the expression in Eqs. (D2) and (D3) and plotted in Figs. 6(a),(b). $\langle \Gamma^\mu_{ij} \rangle$ denotes the ensemble average of MC samples obtained by the lattice average with $(1/N_B)\sum_{ij}$. For the bulk coefficients inside the surface, the number N_B in Eqs. (D3) and (D4) is changed to the total number of bulk bonds. A large difference between $\Gamma^{\rm r}$ and $\Gamma^{\theta,z}$

is observed in the sky phase. To observe the GC effect, in which the surface DMI is smaller than the bulk DMI, the θ, z components $\Gamma^{\theta,z}$(side) obtained on the side surface are plotted in the lower part of Fig. 6(a); the r component is not defined on the side surface. We find that the surface DMI ($=\Gamma^{\theta}$(side)$+\Gamma^{z}$(side)) is remarkably smaller than the bulk DMI ($=\Gamma^{\rm r}+\Gamma^{\theta}+\Gamma^{z}$) in the sky phase (see Appendix C for this difference in DMI). This dynamical enhancement of the surface effects by tensile stress is considered to be an origin of GC effect for skys in nanodots without a magnetic field. In contrast, no apparent difference is observed between the surface DMI ($=\Gamma^{\rm r}$(disk)) on the upper/lower disk and the bulk DMI ($=\Gamma^{\rm r}$). The other components $\Gamma^{\theta,z}$(disk), which are not plotted, are also comparable to the bulk ones $\Gamma^{\theta,{\rm z}}$.

Note that $\Gamma^{\mu}=\langle\Gamma^{\mu}_{ij}\rangle, (\mu=r,\theta,z)$ are considered to be the μ component of a DMI vector [2–6] (Appendeix E). We find that $\Gamma^{\mu}, (\mu=r,\theta,z)$ increase with increasing f and this behavior is qualitatively consistent with the reported result that $D_{\rm ave}$ decreases with increasing strain in Ref. [20], where $D_{\rm ave}$ corresponds to $-\Gamma\left(=-\langle\Gamma_{ij}\rangle=-\Gamma^{\rm r}-\Gamma^{\theta}-\Gamma^{z}\right)$ except for the multiplicative constant D. We also find from Fig. 6(b) that $H^{\mu}_{\rm DM}$ increase ($H^{\mu}_{\rm FM}$ decrease) as f increases in the sky phase representing a competing nature of the interactions necessary for sky emergence. Note that a small discontinuity in $H^{\theta}_{\rm DM}$ at the phase boundary between the sky and stripe indicates a weak first-order transition (Fig. 6(b)). $H^{z}_{\rm DM}$ is (not plotted) close to $H^{\theta}_{\rm DM}$ though it has no discontinuity.

The coefficients $\Omega^{\mu}=\langle\Omega^{\mu}_{ij}\rangle$ and the corresponding $H^{\mu}_{\rm ME}$, which are given by the same expressions for $H^{\mu}_{\rm DM}$ in (D3), are plotted in Figs. 6(c),(d). The symbol $\Omega^{z}_{\rm eff}$ denotes an effective coupling constant defined by

$$\Omega^{z}_{\rm eff}=\alpha f\Omega^{z}, \tag{5}$$

in which the constant α is included. This $\Omega^{z}_{\rm eff}$ is considered to be corresponding to the magnetic anisotropy $K_{\rm ave}$ in Ref. [20], because the z component of $H_{\rm ME}$ also plays a role in the magnetic anisotropy in our model. Thus, we find a qualitative consistency between the observation that $\Omega^{z}_{\rm eff}$ increases with increasing f and the behavior in $K_{\rm ave}$ vs. strain in Ref. [20]. Note that $\Omega^{z}_{\rm eff}\to 0$ for $f\to 0$, and therefore no spontaneous magnetic anisotropy is implemented in the model, as mentioned in Section II B; all anisotropies are dynamically generated and can be evaluated.

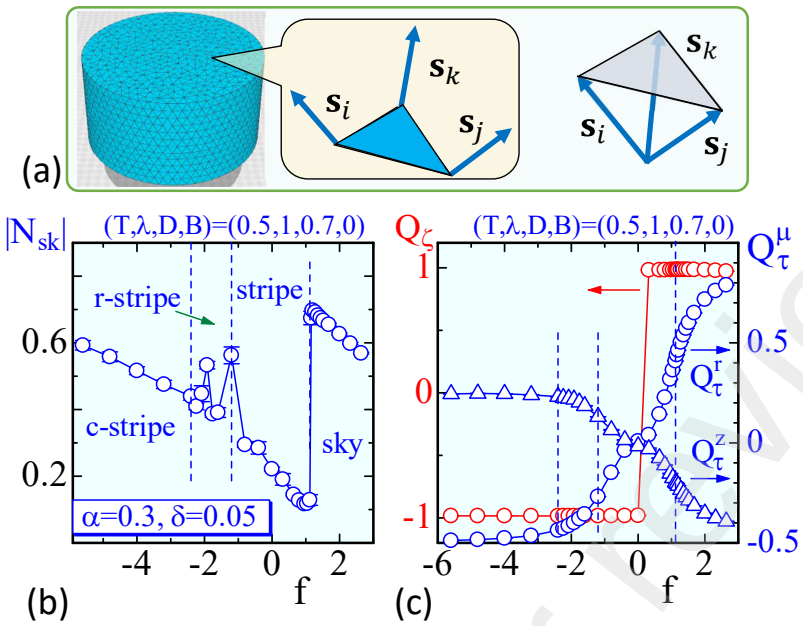

FIG. 7. (a) A triangle ijk and the spins $\mathbf{s}_i$, $\mathbf{s}_j$ and $\mathbf{s}_k$ for the calculation of the topological charge $N_{\rm sk}$ on the upper disk. (b) $|N_{\rm sk}|$ vs. f and (c) order parameters Q_ζ and $Q_\tau^\mu(\mu = r, z)$ vs. f.

The topological charge $N_{\rm sk} = \frac{1}{4\pi}\int d^2x\, \mathbf{s}\cdot\frac{\partial \mathbf{s}}{\partial x^1}\times\frac{\partial \mathbf{s}}{\partial x^2}$ is calculated using the discrete expression

$$N_{\rm sk} = \frac{1}{4\pi}\sum_{\Delta(ijk)} \mathbf{s}_i\cdot(\mathbf{s}_j-\mathbf{s}_i)\times(\mathbf{s}_k-\mathbf{s}_i) \tag{6}$$

on the upper disk of the lattice, where $\Delta(ijk)$ denotes a triangle with vertices i, j and k (see Fig. 7(a)). We observe a topological phase transition between the sky and stripe phases (Fig. 7(b)), although $|N_{\rm sk}|$ is smaller than $|N_{\rm sk}| = 1$ in the sky phase owing to numerical errors originating from discretization. The other reason for $|N_{\rm sk}| < 1$ is that the sign of s^z in the peripheral region is not completely opposite to that in the center. The order of the transition is considered to be first-order if we employ the definition of the first-order transition such that there exists a physical quantity that is discontinuously changing. Moreover, $|N_{\rm sk}|$ in the sky phase is larger than $|N_{\rm sk}|(=0.5)$ of the vortex, implying that the sky configurations under tensile stress are different from those of vortices, as emphasized in Section III C.

An order parameter Q_ζ for ζ defined by

$$Q_\zeta = (1/N_B)\sum_a \zeta_a, \tag{7}$$

is plotted in Fig. 7(c). The value $Q_\zeta = 1$ ($Q_\zeta = -1$) corresponds to the cosine (sine) type v_{ij} in Eq. (C2). The abrupt change in Q_ζ at $f = 0$ indicates an internal phase transition for

Finsler length caused by external mechanical stress f. Notably, we verified that no c-stripe configuration emerges if $Q_\zeta = 1 (\Leftrightarrow v_{ij} = |\cos\theta_{ij}| + v_0)$ for $f < 0$ by manually fixing ζ to be $\zeta = 1$. Therefore, this transition (Fig 7(b)) in the Finsler length is expected to be crucial for the morphological change on nanodots under radial stress. From the direction-dependent nonpolar order parameters $Q^\mu_\tau = \frac{3}{2}\left(\langle(\vec{\tau}\cdot\vec{e}^{\,\mu}_i)^2\rangle - \frac{1}{3}\right)$, $(\mu = r, z)$ in Fig. 7(c), we find that the strain $\vec{\tau}$ is at random $(\Leftrightarrow Q^\mu_\tau \to 0, (\mu = r, z))$ for $f \to 0$ and aligns such that $\tau^r \to 0$ $(\tau^z \to 0)$ in the c-stripe (sky) phase, as expected.

IV. CONCLUDING REMARKS

In this paper, we numerically study skyrmion (sky) stability in nanodots with and without a magnetic field using the Finsler geometry (FG) modeling technique and find that a single sky is stabilized at the center of a radially emerged strain field under radial stress. Metropolis Monte Carlo technique is used for the simulations on 3D tetrahedral lattices of cylindrical shape. Our Hamiltonian is defined with the variables of electric spins and strain direction, and an Ising-like variable to dynamically treat the anisotropy of the magneto-elastic coupling (MEC) in FG modeling.

For the GC effect without stress, we confirm that the minimal external magnetic field for the skys decreases when the nanodot diameter decreases, which is consistent with previously reported experimental data by Wang et al. When radial stresses are applied under a zero magnetic field, we confirm two different morphological phases, the sky and stripe, by varying the stress from positive (tension) to negative (compression). A stable sky emerges at the center of the nanodot owing to the surface effect dynamically enhanced by the strains. The stripe phase can be divided into three phases: stripe and circular stripes and one intermediate phase between the stripe and circular stripe phases. This morphological change in response to stress is also consistent with previously reported experimental results. Thus, we consider that the origins of sky stability on nanodots without a magnetic field are (i) dynamically enhanced surface effect for GC and (ii) dynamically generated interaction anisotropies of FMI, DMI, and MEC under radial stresses.

ACKNOWLEDGMENTS

This work is supported in part by Collaborative Research Project J23Ly07 of the Institute of Fluid Science (IFS), Tohoku University. Numerical simulations were performed on the supercomputer system AFI-NITY at the Advanced Fluid Information Research Center, IFS, Tohoku University.

Appendix A: Lattice construction

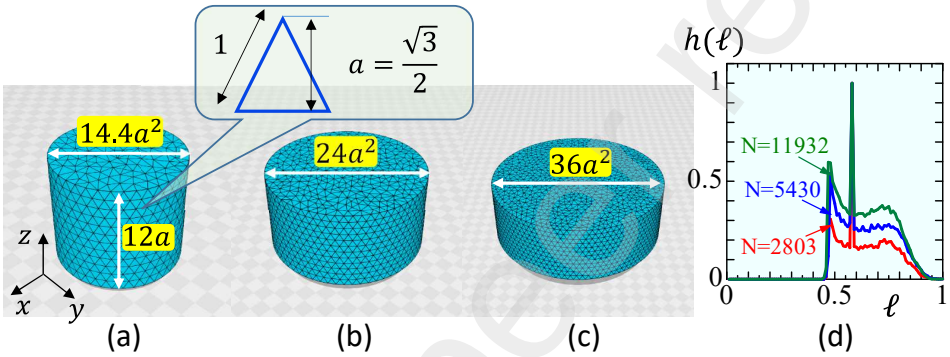

FIG. 8. Cylindrical lattices of size (a) $N = 2803$, (b) $N = 5430$ and (c) $N = 11932$ composed of tetrahedrons. The diameters are $d = 14.4a^2$, $d = 24a^2$, and $d = 36a^2$ in (a), (b) and (c), respectively, while the height is fixed to $h = 12a$, where $a(= \sqrt{3}/2)$ is the height of a regular triangle of unit edge-length on the cylindrical surface. (d) Distribution $h(\ell)$ of bond length ℓ, where both $h(\ell)$ and ℓ are normalized. The peak at $\ell \simeq 0.6$ corresponds to the bond of the cylindrical surface. The height shares the symbol h with the distribution $h(\ell)$, however, no confusion is expected.

The height h of the cylinder is fixed to $h = 12a$ (Fig. 8), and the diameter d is determined by the ratio $R = d/h$. We plot three cylinders of $R = 1.2a$, $R = 2a$ and $R = 3a$ in Figs. 8(a)–(c). The cylindrical surface is composed of a regular triangle. The total number of vertices on each of the top and bottom disks, including the edge, is given by $\pi(d/2)^2/(\sqrt{3}/2)$, where $\sqrt{3}/2$ is the area of two regular triangles and the vertices are randomly distributed as uniformly as possible. The distribution of vertices on the upper disk is the same as that on the bottom disk. The vertices inside the surface are also randomly distributed as uniformly as possible, and the total number is calculated using the volume of vertices inside the surface, in which the space is assumed to be filled with regular tetrahedrons. Vertex

TABLE I. Lattices are characterized by the numbers $N, N_B, N_T, N_{\rm tet}$, which are the total number of vertices, bonds, triangles, and tetrahedrons. The Euler number $\chi(=N-N_B+N_T-N_{\rm tet})$ satisfies $\chi=1$, implying that the lattices are filled with tetrahedrons. Diameter d and ratio $R(=d/h)$ characterize the lattice shapes. The height h of the cylinder is $h=12a$ (Fig. 8).

N	N_B	N_T	$N_{\rm tet}$	χ	d	$R(=d/h)$
2083	13686	22501	10897	1	$14.4a^2$	$1.2a$
5430	36720	61093	29802	1	$24a^2$	$2a$
8465	57882	96700	47282	1	$30a^2$	$2.5a$
11932	82097	137492	67326	1	$36a^2$	$3a$

volume is calculated as $(\sqrt{2}/48)\times 22.8$, where $(\sqrt{2}/48$ is a quarter of the regular tetrahedron volume and 22.8 is an approximate number of the regular tetrahedrons emanating from the inner vertices calculated by $4\pi/\Omega$ with the solid angle Ω of a vertex of the tetrahedron. The peak of the distributions $h(\ell)$ of the bond length ℓ plotted in 8(d) corresponds to the bond on the cylindrical surface. Table I lists the numbers characterizing the lattices.

The mean value of the total number of tetrahedrons $n_{ij}(=\sum_{\Delta(ij)}1)$ sharing bond ij are shown in Table II. We find that $\frac{\overline{n}(\rm side)}{\overline{n}(\rm bulk)}\simeq 0.51$. This ratio is one of the origins of the surface effect on GC that the surface DMI on the side surface is smaller than the bulk DMI. The surface effect will be described in Appendix C. To show that the direction $\vec{e}_{ij}$ of bond ij is isotropic, the lattice averages $(\vec{e}_{ij}\cdot\vec{e}^{\,r})^2$, $(\vec{e}_{ij}\cdot\vec{e}^{\,\theta})^2$ and $(\vec{e}_{ij}\cdot\vec{e}^{\,z})^2$ are listed. We find from $(\vec{e}_{ij}\cdot\vec{e}^{\,\mu})^2\simeq 1/3, (\mu=r,\theta,z)$ that the bond direction $\vec{e}_{ij}$ is isotropically distributed.

Appendix B: Discrete Hamiltonian

The discrete Hamiltonian in Eq. (1) is

$$H(\mathbf{s},\vec{\tau},\zeta)=\lambda H_{\rm FM}+DH_{\rm DM}+H_B+\alpha H_{\rm ME}+H_f+\delta H_\zeta. \tag{B1}$$

TABLE II. The mean value of the total number of tetrahedrons sharing bond ij are calculated using $\overline{n}=\frac{\sum_{ij}\sum_{\Delta(ij)}1}{\sum_{ij}1}$ on upper and lower disks, side surface and inside, denoted by $\overline{n}$(disk), $\overline{n}$(side) and $\overline{n}$(bulk), respectively. $\overline{n}$ is the mean value for all bonds ij. $(\vec{e}_{ij}\cdot\vec{e}^{\,\mu})^2, (\mu=r,\theta,z)$ are the lattice averages of squared μ components of bond direction $\vec{e}_{ij}$, where $\vec{e}^{\,\mu}(\mu=r,\theta,z)$ denote the (r,θ,z) direction at the center of bond ij (see Appendix D).

N	$\overline{n}$(disk)	$\overline{n}$(side)	$\overline{n}$(bulk)	$\overline{n}$	$(\vec{e}_{ij}\cdot\vec{e}^{\,r})^2$	$(\vec{e}_{ij}\cdot\vec{e}^{\,\theta})^2$	$(\vec{e}_{ij}\cdot\vec{e}^{\,z})^2$
2083	2.85	2.65	5.16	4.78	0.340	0.336	0.330
5430	2.80	2.64	5.17	4.87	0.333	0.330	0.338
8465	2.80	2.65	5.17	4.90	0.329	0.329	0.340
11932	2.80	2.65	5.17	4.92	0.330	0.329	0.342

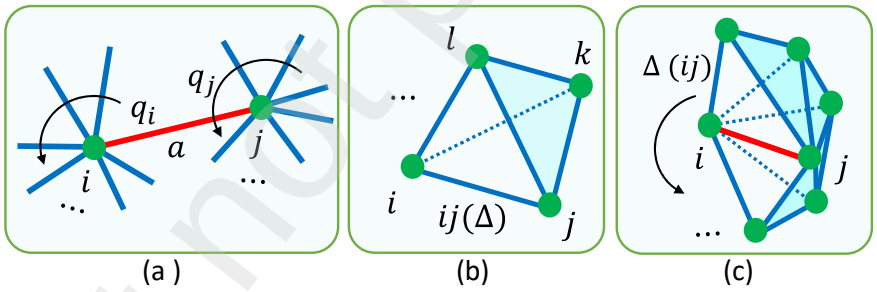

FIG. 9. (a) Illustration of bond a and the connected bonds. The total number of the connected bonds at vertex i (j) is q_i-1 (q_j-1), where q_i (q_j) is the coordination number at vertex i (j). Illustrations of (b) $\sum_{ij(\Delta)}$; the sum over bonds $ij(\Delta)$ of tetrahedron Δ, and (c) $\sum_{\Delta(ij)}$; the sum over tetrahedrons $\Delta(ij)$ sharing bond ij. $\sum_{ij(\Delta)}1=4$ for all Δ, and the number $n_{ij}=\sum_{\Delta(ij)}1$ depends on bond ij.

The terms on the right hand side are given as follows:

$$
\begin{aligned}
&H_{\mathrm{FM}} = \sum_{\Delta} \sum_{ij(\Delta)} \Gamma_{ij}(\vec{\tau}) \left(1 - \mathbf{s}_i \cdot \mathbf{s}_j\right), \quad H_{\mathrm{DM}} = \sum_{\Delta} \sum_{ij(\Delta)} \Gamma_{ij}(\vec{\tau}) \vec{e}_{ij} \cdot \mathbf{s}_i \times \mathbf{s}_j, \\
&H_B = -\sum_i \mathbf{s}_i \cdot \vec{B}, \quad \vec{B} = (0, 0, -B), \\
&H_{\mathrm{ME}} = -f \sum_{\Delta} \sum_{ij(\Delta)} \Omega_{ij}(\vec{\tau}, \zeta) \left(\mathbf{s}_i \cdot \mathbf{s}_j\right)^2, \\
&H_f = -\mathrm{sgn}(f) \sum_i \left(\vec{\tau}_i \cdot \vec{f}\right)^2, \quad \vec{f} = f \frac{\vec{r}}{\|\vec{r}\|}, \quad \mathrm{sgn}(f) = \begin{cases} 1 & (f > 0) \\ -1 & (f < 0) \end{cases}, \\
&H_\zeta = -\sum_{(ab)} \zeta_a \zeta_b
\end{aligned}
\tag{B2}
$$

The first term H_{FM} is an FMI energy that is deformed to have a $\vec{\tau}$-dependent interaction coefficient $\Gamma_{ij}(\vec{\tau})$ (see Appendix C for FG modeling details). The second term is also the deformed DMI energy with the same $\Gamma_{ij}(\vec{\tau})$. The third term H_B is the Zeeman energy and the fourth term is the energy for the ME coupling quadratic with respect to $\mathbf{s}$ with a coefficient $\Omega_{ij}(\vec{\tau}, \zeta)$, which is dynamically changeable and different from $\Gamma_{ij}(\vec{\tau})$ in H_{FM} and H_{DM} (Appendix C). The fifth term H_f denotes the energy for the response of strain $\vec{\tau}$ to an external stress $\vec{f}$ along the radial direction. The final term is defined as the sum of connected bonds a and b denoted by (ab) (Fig. 9(a)). We note that H_ζ is equivalent to the Potts model Hamiltonian, $H_{\mathrm{P}} = -\sum_{ab} \delta_{\zeta_a,\zeta_b}$, where $\delta_{\zeta_a,\zeta_b} = 1$ $(\zeta_a = \zeta_b)$ and $\delta_{\zeta_a,\zeta_b} = 0$ $(\zeta_a \neq \zeta_b)$. H_{FM}, H_{DM} and H_{ME} are commonly defined by $\sum_\Delta \sum_{ij(\Delta)}$, the sum over tetrahedrons Δ, where $\sum_{ij(\Delta)}$ denotes the sum over bonds $ij(\Delta)$ of tetrahedron Δ (Fig. 9(b)).

Appendix C: Discretization of direction-dependent interaction coefficient

Finsler geometry framework provides interaction anisotropy between two particles via a direction-dependent Finsler length v_{ij} (Fig. 10(a)). The Finsler length v_{ij} for $H_{\mathrm{FM}}, H_{\mathrm{DM}}$ is fixed to be cosine type, and v_{ij} for H_{ME} is defined to be changeable to cosine type or sine type depending on ζ_{ij} $(\in \{-1, 1\}$ on bond $ij)$:

$$
v_{ij} = |\cos\theta_{ij}| + v_0, \quad (v_0 = 0.1;\ H_{\mathrm{FM}}, H_{\mathrm{DM}}) \tag{C1}
$$

$$
v_{ij} = \begin{cases} |\cos\theta_{ij}| + v_0, & (\zeta_{ij} = 1) \\ \sin\theta_{ij} + v_0, & (\zeta_{ij} = -1) \end{cases}, (v_0 = 0.2;\ H_{\mathrm{ME}}), \tag{C2}
$$

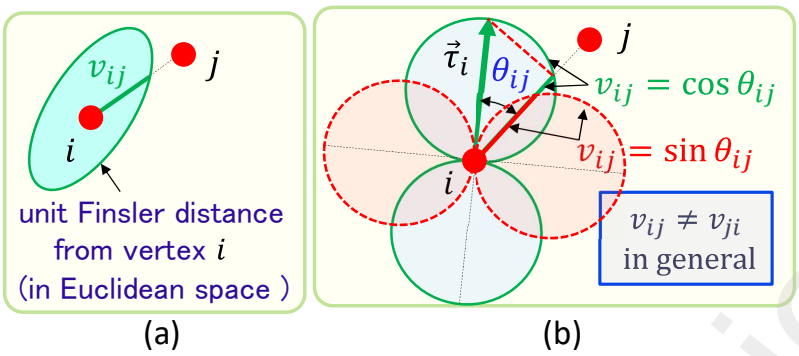

FIG. 10. (a) Trajectory of unit Finsler length v_{ij} at i is not always spherical or symmetric in Euclidean space, (b) the trajectory for v_{ij} assumed in this paper, which depends on strain direction $\vec{\tau}_i (\in S^2/2)$. Note that $v_{ij} \neq v_{ji}$ because $\vec{\tau}_i \neq \vec{\tau}_j$ in general (Eq. (C3)).

where $\cos\theta_{ij}$ and $\sin\theta_{ij}$ (Fig. 10(b)) are

$$\cos\theta_{ij} = \vec{\tau}_i \cdot \vec{e}_{ij}, \quad \sin\theta_{ij} = \sqrt{1 - |\vec{\tau}_i \cdot \vec{e}_{ij}|^2}\ (\geq 0), \tag{C3}$$

and v_0 is a small cutoff.

Using these v_{ij}, the Finsler metric is defined by

$$g_{ab} = \begin{pmatrix} v_{12}^{-2} & 0 & 0 \\ 0 & v_{13}^{-2} & 0 \\ 0 & 0 & v_{14}^{-2} \end{pmatrix}, \quad \sqrt{g} = \sqrt{\det g_{ab}} = v_{12}^{-1} v_{13}^{-1} v_{14}^{-1}, \quad g^{ab} = (g_{ab})^{-1}. \tag{C4}$$

These expressions are used to obtain the discrete Hamiltonian in Eq. (B2) from the continuous ones

$$\begin{aligned} H_{\rm FM} &= \frac{1}{2} \int \sqrt{g} d^3x g^{ab} \frac{\partial \mathbf{s}}{\partial x^a} \cdot \frac{\partial \mathbf{s}}{\partial x^b}, \\ H_{\rm DM} &= \int \sqrt{g} d^3x g^{ab} \frac{\partial \vec{r}}{\partial x^a} \cdot \mathbf{s} \times \frac{\partial \mathbf{s}}{\partial x^b}, \\ H_{\rm ME} &= \frac{1}{4} \int \sqrt{g} d^3x \left(g^{ab} \frac{\partial \mathbf{s}}{\partial x^a} \cdot \frac{\partial \mathbf{s}}{\partial x^b} \right)^2, \end{aligned} \tag{C5}$$

by replacing the differentials with differences such that $\partial_1 \mathbf{s} \to \mathbf{s}_2 - \mathbf{s}_1$, $\partial_2 \mathbf{s} \to \mathbf{s}_3 - \mathbf{s}_1$ and $\partial_3 \mathbf{s} \to \mathbf{s}_4 - \mathbf{s}_1$ for a local coordinate system with the origin at the vertex 1, and by replacing $\int \sqrt{g} d^3x$ with the sum over tetrahedrons $\sum_\Delta$ and the sum over bonds $\sum_{ij(\Delta)}$ of the tetrahedron Δ, and by summing over all symmetric expressions obtained by the cyclic replacements $1 \to 2, 2 \to 3, 3 \to 4, 4 \to 1$ (Fig. 1(c)). For the discrete $H_{\rm ME}$, only quadratic terms such as $(\mathbf{s}_i \cdot \mathbf{s}_j)^2$ in the expansion of $\left(g^{ab} \frac{\partial \mathbf{s}}{\partial x^a} \cdot \frac{\partial \mathbf{s}}{\partial x^b}\right)^2$ are used.

In these discrete calculations, we extract an intensive part of the energies, the so-called position- and direction-dependent coupling constants

$$\Gamma_{ij} = \hat{\Gamma}^{-1}\gamma_{ij}, \quad \hat{\Gamma} = \bar{n}\,\langle\gamma_{ij}^{\rm iso}\rangle, \tag{C6}$$

$$\begin{aligned}
\gamma_{12} &= \frac{v_{12}^3}{v_{13}v_{14}} + \frac{v_{21}^3}{v_{23}v_{24}}, \quad \gamma_{13} = \frac{v_{13}^3}{v_{12}v_{14}} + \frac{v_{31}^3}{v_{32}v_{34}}, \\
\gamma_{14} &= \frac{v_{14}^3}{v_{13}v_{14}} + \frac{v_{41}^3}{v_{42}v_{43}}, \quad \gamma_{23} = \frac{v_{23}^3}{v_{21}v_{24}} + \frac{v_{32}^3}{v_{31}v_{34}}, \\
\gamma_{24} &= \frac{v_{24}^3}{v_{21}v_{23}} + \frac{v_{42}^3}{v_{41}v_{43}}, \quad \gamma_{34} = \frac{v_{34}^3}{v_{31}v_{32}} + \frac{v_{43}^3}{v_{41}v_{42}}.
\end{aligned} \tag{C7}$$

Here, we describe only Γ_{ij} for simplicity, because the difference between Γ_{ij} and Ω_{ij} is only v_{ij} in Eqs. (C1) and (C2). In Eq. (C6), $\bar{n}(=\frac{\sum_{\Delta(ij)}1}{\sum_{ij}1})$ denotes the mean value of $n_{ij}=\sum_{\Delta(ij)}1$, which is the total number of tetrahedrons Δ sharing bond ij (Fig. 9(c)), and $\langle\gamma_{ij}^{\rm iso}\rangle$ denotes the mean value of the lattice average $\frac{\sum_\Delta\sum_{ij(\Delta)}\gamma_{ij}}{\sum_\Delta\sum_{ij(\Delta)}1}$ of γ_{ij} calculated with 1000 isotropic configurations of $\vec{\tau}$. Note that the random configurations to obtain $\langle\gamma_{ij}^{\rm iso}\rangle$ for Ω_{ij} include randomly distributed ζ on the bonds. The reason for introducing the v_0-dependent factor $\langle\gamma_{ij}^{\rm iso}\rangle^{-1}$ is that γ_{ij} varies depending on v_0's in Eqs. (C1) and (C2) even for the isotropic case, and the parameters λ and D should be changed to obtain a spin configuration similar to the original one when v_0's are changed if $\langle\gamma_{ij}^{\rm iso}\rangle^{-1}$ is not included.

We briefly show the surface effect for GC. There are two possible sources; static and dynamical, for the surface effect. One comes from the lattice structure and the other from a dynamical effect in FG modeling. The first one, which is the static part, is shown using the coupling constant in Eq. (C6) as follows. It is noteworthy that the lattice average $\overline{\Gamma}=\frac{\sum_\Delta\sum_{ij(\Delta)}\Gamma_{ij}}{\sum_\Delta\sum_{ij(\Delta)}1}$ of Γ_{ij} for an isotropic configuration of $\vec{\tau}$ satisfy $\overline{\Gamma}(=\overline{\Gamma}_{ij})\simeq\bar{n}^{-1}$. Let γ_{ij} be a coefficient obtained with an isotropic configuration of $\vec{\tau}$ and $\overline{\gamma}_{ij}$ be the lattice average. Then, we have that $\overline{\Gamma}=\bar{n}^{-1}\langle\gamma_{ij}^{\rm iso}\rangle^{-1}\overline{\gamma}_{ij}=\frac{1}{\bar{n}\langle\gamma_{ij}^{\rm iso}\rangle}\frac{\sum_\Delta\sum_{ij(\Delta)}\gamma_{ij}}{\sum_\Delta\sum_{ij(\Delta)}1}\simeq\bar{n}^{-1}$ because the lattice average $\overline{\gamma}_{ij}(=\frac{\sum_\Delta\sum_{ij(\Delta)}\gamma_{ij}}{\sum_\Delta\sum_{ij(\Delta)}1})$ of isotropic γ_{ij} is close to $\langle\gamma_{ij}^{\rm iso}\rangle$. Using $\overline{\Gamma}$, the Hamiltonian of DMI in Eq. (B2) for isotropic $\vec{\tau}$ can be written as

$$\begin{aligned}
H_{\rm DM} &= \sum_\Delta\sum_{ij(\Delta)}\Gamma_{ij}\vec{e}_{ij}\cdot\mathbf{s}_i\times\mathbf{s}_j \\
&\to \sum_\Delta\sum_{ij(\Delta)}\overline{\Gamma}\vec{e}_{ij}\cdot\mathbf{s}_i\times\mathbf{s}_j = \bar{n}^{-1}\sum_{ij}\sum_{\Delta(ij)}\vec{e}_{ij}\cdot\mathbf{s}_i\times\mathbf{s}_j \\
&= \sum_{ij}(\bar{n}^{-1}\sum_{\Delta(ij)}1)\vec{e}_{ij}\cdot\mathbf{s}_i\times\mathbf{s}_j = \sum_{ij}(n_{ij}/\bar{n})\vec{e}_{ij}\cdot\mathbf{s}_i\times\mathbf{s}_j,
\end{aligned} \tag{C8}$$

where Γ_{ij} is replaced by $\overline{\Gamma}$ and the summation convention $\sum_{ij}\sum_{\Delta(ij)}=\sum_{\Delta}\sum_{ij(\Delta)}$ is used. The replacement of Γ_{ij} with a constant $\overline{\Gamma}$ is to neglect all dynamical effects implemented by FG modeling and to leave only contribution from the lattice structure. This form of $H_{\rm DM}=\sum_{ij}(n_{ij}/\bar{n})\vec{e}_{ij}\cdot\mathbf{s}_i\times\mathbf{s}_j$ includes the weight $n_{ij}/\bar{n}$, which modifies the interaction $\vec{e}_{ij}\cdot\mathbf{s}_i\times\mathbf{s}_j$ to be dependent on the position of bond ij whether it is on the surface or inside. The number $n_{ij}=\sum_{\Delta(ij)}1$ is small (large) on the surface (bulk) (Table II and Fig. 9(c)). Thus, we confirm that this weight difference is one possible origin of the surface effect in the small strain region $f\to 0$, where $\vec{\tau}$ is isotropic. The GC effect at $f=0$ is confirmed in Section III A.

When an anisotropic configuration of $\vec{\tau}$ (and ζ) is reflected in γ_{ij}, the weight difference is further enlarged in the region of $f>0$ in the sky phase (Fig. 6(a)). This enlargement dynamically caused by $\vec{\tau}$ is the dynamical part of the surface effect for GC. Here, we should emphasize that the surface effect on the difference in the interaction weight in $H_{\rm DM}$, caused by both lattice itself and $\vec{\tau}$ dynamics, is considered to be the origin of the GC effect for skys in nanodots under strains [28].

Appendix D: Decomposition of interaction coefficient and the corresponding energies

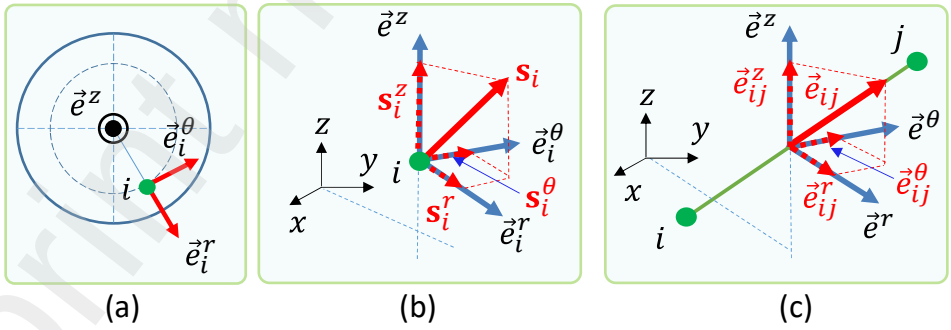

FIG. 11. (a) Polar coordinate position of vertex i. The coordinate origin is at the center of nanodot. (b) Spin vector $\mathbf{s}_i$ is decomposed into the radial $\vec{e}_i^{\,r}$, tangential $\vec{e}_i^{\,\theta}$ and $\vec{e}^{\,z}$ directions at vertex i, where $\mathbf{s}_i^{\mu}=(\mathbf{s}_i\cdot\vec{e}_i^{\,\mu})\vec{e}_i^{\,\mu},(\mu=r,\theta,z)$. (c) The unit vector $\vec{e}_{ij}$ from vertices i to j can be decomposed into the $\vec{e}^{\,r}$, $\vec{e}^{\,\theta}$ and $\vec{e}^{\,z}$ components, where $\vec{e}^{\,r}$ and $\vec{e}^{\,\theta}$ are given by Eq. (D1) and $\vec{e}_{ij}^{\,\mu}=(\vec{e}_{ij}\cdot\vec{e}^{\,\mu})\vec{e}^{\,\mu},(\mu=r,\theta,z)$.

Let $\vec{e}_{ij}$ be the unit vector from vertices i to j and $\vec{e}_i^{\,r}$, $\vec{e}_i^{\,\theta}$ and $\vec{e}^{\,z}$ be the unit vectors along the r, θ and z directions at the vertex i as illustrated in Figs. 11(a),(b), where the coordinate origin is at the center of nanodot and $\vec{e}_i^{\,z}$ is independent of i and written as $\vec{e}^{\,z}$. Here, we define unit vectors

$$\vec{e}^{\,\mu} = \frac{1}{2}\left(\vec{e}_i^{\,\mu} + \vec{e}_j^{\,\mu}\right), \quad (\mu = r, \theta) \tag{D1}$$

to represent the r and θ directions at the center of bond ij (Fig. 11(c)). Then, we have a decomposition of $\vec{e}_{ij}$ such that $\vec{e}_{ij} = (\vec{e}_{ij}\cdot\vec{e}^{\,r})\vec{e}^{\,r} + (\vec{e}_{ij}\cdot\vec{e}^{\,\theta})\vec{e}^{\,\theta} + (\vec{e}_{ij}\cdot\vec{e}^{\,z})\vec{e}^{\,z}$. Using the expressions $1 = \vec{e}_{ij}\cdot\vec{e}_{ij} = (\vec{e}_{ij}\cdot\vec{e}^{\,r})^2 + (\vec{e}_{ij}\cdot\vec{e}^{\,\theta})^2 + (\vec{e}_{ij}\cdot\vec{e}^{\,z})^2$ and $\Gamma_{ij} = \Gamma_{ij}\left((\vec{e}_{ij}\cdot\vec{e}^{\,r})^2 + (\vec{e}_{ij}\cdot\vec{e}^{\,\theta})^2 + (\vec{e}_{ij}\cdot\vec{e}^{\,z})^2\right)$, we have a decomposition of $\Gamma_{ij}(\vec{\tau})$ such that

$$\Gamma_{ij}^r(\vec{\tau}) = \Gamma_{ij}(\vec{\tau})(\vec{e}_{ij}\cdot\vec{e}^{\,r})^2, \quad \Gamma_{ij}^\theta(\vec{\tau}) = \Gamma_{ij}(\vec{\tau})(\vec{e}_{ij}\cdot\vec{e}^{\,\theta})^2, \quad \Gamma_{ij}^z(\vec{\tau}) = \Gamma_{ij}(\vec{\tau})(\vec{e}_{ij}\cdot\vec{e}^{\,z})^2. \tag{D2}$$

This decomposition of "scalar function" Γ_{ij} corresponds to the decomposition of DMI vector (Appendix E) and is considered a physically meaningful decomposition. Using these direction-dependent coefficients, the corresponding energies $H_{\rm FM}$, $H_{\rm DM}$, $H_{\rm ME}$ can also be decomposed into direction-dependent energies. Here, we show the decomposition of H_{DM}:

$$\begin{aligned}
H_{\rm DM}^r &= \frac{\sum_\Delta \sum_{ij(\Delta)} \Gamma_{ij}^r(\vec{\tau})\vec{e}_{ij}\cdot\mathbf{s}_i\times\mathbf{s}_j}{\frac{1}{N_B}\sum_\Delta\sum_{ij(\Delta)}\Gamma_{ij}^r}, \\
H_{\rm DM}^\theta &= \frac{\sum_\Delta \sum_{ij(\Delta)} \Gamma_{ij}^\theta(\vec{\tau})\vec{e}_{ij}\cdot\mathbf{s}_i\times\mathbf{s}_j}{\frac{1}{N_B}\sum_\Delta\sum_{ij(\Delta)}\Gamma_{ij}^\theta}, \\
H_{\rm DM}^z &= \frac{\sum_\Delta \sum_{ij(\Delta)} \Gamma_{ij}^z(\vec{\tau})\vec{e}_{ij}\cdot\mathbf{s}_i\times\mathbf{s}_j}{\frac{1}{N_B}\sum_\Delta\sum_{ij(\Delta)}\Gamma_{ij}^z},
\end{aligned} \tag{D3}$$

where the factor $1/N_B, N_B = \sum_{ij} 1$ the total number of bonds, is multiplied to obtain the mean value of $\Gamma_{ij}^\mu (\mu = r, \theta, z)$ per bond. The denominators on the right hand side are the lattice averages of the components in Eq. (D2). Using these expressions, we have

$$\begin{aligned}
H_{\rm DM} &= \sum_\Delta\sum_{ij(\Delta)} \Gamma_{ij}(\vec{\tau})\vec{e}_{ij}\cdot\mathbf{s}_i\times\mathbf{s}_j = \sum_\Delta\sum_{ij(\Delta)}\left(\Gamma_{ij}^r + \Gamma_{ij}^\theta + \Gamma_{ij}^z\right)\vec{e}_{ij}\cdot\mathbf{s}_i\times\mathbf{s}_j \\
&= \left(\frac{1}{N_B}\sum_\Delta\sum_{ij(\Delta)}\Gamma_{ij}^r(\vec{\tau})\right) H_{\rm DM}^r + \left(\frac{1}{N_B}\sum_\Delta\sum_{ij(\Delta)}\Gamma_{ij}^\theta(\vec{\tau})\right) H_{\rm DM}^\theta + \left(\frac{1}{N_B}\sum_\Delta\sum_{ij(\Delta)}\Gamma_{ij}^z(\vec{\tau})\right) H_{\rm DM}^z,
\end{aligned} \tag{D4}$$

and therefore, the mean value is given by

$$\langle H_{\rm DM}\rangle = \langle\Gamma_{ij}^r\rangle\langle H_{\rm DM}^r\rangle + \langle\Gamma_{ij}^\theta\rangle\langle H_{\rm DM}^\theta\rangle + \langle\Gamma_{ij}^z\rangle\langle H_{\rm DM}^z\rangle, \tag{D5}$$

where $\langle * \rangle$ denotes the sample or ensemble average calculated via MC simulations. We should note that $H_{\rm FM}$ in Eq. (B2) is obtained from $H_{\rm DM}$ by replacing $\mathbf{s}_i \times \mathbf{s}_j$ with $\vec{e}_{ij}(1-\mathbf{s}_i \cdot \mathbf{s}_j)$. Therefore, the directional dependence of $1-\mathbf{s}_i \cdot \mathbf{s}_j$ along $\vec{e}_{ij}$ can also be evaluated with the same procedure for $H_{\rm DM}$. $H_{\rm ME}$ is treated in the same manner.

Appendix E: DMI vector

Effective coupling constants $\Gamma_{ij}^{\mu}(\vec{\tau}),\ (\mu = r, \theta, z)$ are understood to be μ components of a DMI vector. First, $H_{\rm DM}$ can be written as

$$H_{\rm DM} = \sum_{ij} \mathbf{D}_{ij} \cdot \mathbf{s}_i \times \mathbf{s}_j, \tag{E1}$$

where $\mathbf{D}_{ij}$ is a DMI vector and $\sum_{ij}$ denotes the sum over bonds ij. Second, $H_{\rm DM}$ in Eq. (B2) can be expressed by the sum over bonds:

$$H_{\rm DM} = \sum_{ij} \sum_{\Delta(ij)} \Gamma_{ij}(\vec{\tau}) \vec{e}_{ij} \cdot \mathbf{s}_i \times \mathbf{s}_j, \tag{E2}$$

where $\sum_{\Delta(ij)}$ denotes the sum over tetrahedrons sharing bond ij. The expression in Eq. (E2) is obtained from $H_{\rm DM}$ in Eq. (B2) by using the identity $\sum_{\Delta} \sum_{ij(\Delta)} = \sum_{ij} \sum_{\Delta(ij)}$. Therefore, comparing Eqs. (E1) and (E2), we obtain

$$\begin{aligned} \mathbf{D}_{ij} &= \sum_{\Delta(ij)} \Gamma_{ij}(\vec{\tau}) \vec{e}_{ij} \\ &= \sum_{\Delta(ij)} \Gamma_{ij}(\vec{\tau}) \left[(\vec{e}_{ij} \cdot \vec{e}^{\,r}) \vec{e}^{\,r} + (\vec{e}_{ij} \cdot \vec{e}^{\,\theta}) \vec{e}^{\,\theta} + (\vec{e}_{ij} \cdot \vec{e}^{\,z}) \vec{e}^{\,z} \right], \end{aligned} \tag{E3}$$

and the μ component

$$D_{ij}^{\mu} = \mathbf{D}_{ij} \cdot \vec{e}^{\,\mu} = \sum_{\Delta(ij)} \Gamma_{ij}(\vec{\tau}) (\vec{e}_{ij} \cdot \vec{e}^{\,\mu})^2,\ (\mu = r, \theta, z), \tag{E4}$$

where $\vec{e}^{\,\mu}$ denotes the μ component of $\vec{e}_{ij}$ (see Eq. (D1) and Fig. 11(c)). From the mean value by the lattice average with $(1/N_B) \sum_{ij}$ and ensemble average, we have

$$\begin{aligned} \langle D_{ij}^{\mu} \rangle &= \langle \frac{1}{N_B} \sum_{ij} \sum_{\Delta(ij)} \Gamma_{ij}(\vec{\tau}) \rangle (\vec{e}_{ij} \cdot \vec{e}^{\,\mu})^2 \\ &= \langle \frac{1}{N_B} \sum_{\Delta} \sum_{ij(\Delta)} \Gamma_{ij}(\vec{\tau}) \rangle (\vec{e}_{ij} \cdot \vec{e}^{\,\mu})^2 \\ &= \langle \Gamma_{ij}^{\mu}(\vec{\tau}) \rangle,\ (\mu = r, \theta, z). \end{aligned} \tag{E5}$$

If we write $D^{\mu} = \langle D^{\mu}_{ij} \rangle$, then $\Gamma^{\mu} (= \langle \Gamma^{\mu}_{ij} \rangle)$ in Fig. 6(a) is identified with D^{μ}. Using D^{μ}, Eq. (D5) can also be written as $\langle H_{\rm DM} \rangle = D^{r} \langle H^{r}_{\rm DM} \rangle + D^{\theta} \langle H^{\theta}_{\rm DM} \rangle + D^{z} \langle H^{z}_{\rm DM} \rangle$. Therefore, the extensive parts $\langle H^{\mu}_{\rm DM} \rangle, (\mu = r, \theta, z)$ are considered to be physically meaningful direction-dependent energies as a response to the intensive parts D^{μ}.

---

[1] N. Romming, C. Hanneken, M. Menzel, J. E. Bickel, B. Wolter, K. von Bergmann, A. Kubetzka and R. Wiesendanger, *Writing and deleting single magnetic skyrmions*, Science **341** (6146), 636-639 (2013), https://doi.org/10.1126/science.1240573.

[2] A. Fert, N. Reyren and V. Cros, *Magnetic skyrmions: advances in physics and potential applications*, Nature Reviews **2**, 17031 (2017), https://doi.org/10.1038/natrevmats.2017.31.

[3] X. Zhang, Y. Zhou, K. M. Song, T.-E. Park, J. Xia, M. Ezawa, X. Liu, W. Zhao, G. Zhao and S. Woo, *Skyrmion-electronics: writing, deleting, reading and processing magnetic skyrmions toward spintronic applications*, J. Phys.: Condens. Matter **32** 143001 (2020), https://doi.org/10.1088/1361-648X/ab5488.

[4] Y. Tokura and N. Kanazawa, *Magnetic Skyrmion Materials*, Chem. Rev. **121**, 5, pp. 2857–2897 (2021), https://doi.org/10.1021/acs.chemrev.0c00297.

[5] Börge Göbel, I. Mertig, O. A. Tretiakov, *Beyond skyrmions: Review and perspectives of alternative magnetic quasiparticles*, Phys. Rep. **895** 1-28, (2021), https://doi.org/10.1016/j.physrep.2020.10.001.

[6] K. Wang, V. Bheemarasetty, J. Duan, S. Zhou and G. Xiao, *Fundamental physics and applications of skyrmions: A review*, J. Mag. Mag. Mat. **563**, 169905 (2022), https://doi.org/10.1016/j.jmmm.2022.169905.

[7] Sheng Li, Xuewen Wang, Theo Rasing, *Magnetic skyrmions: Basic properties and potential applications*, Interdisciplinary Materials **563**, 169905 (2022), https://doi.org/10.1002/idm2.12072.

[8] M. Uchida, Y. Onose,Y. Matsui and Y. Tokura, *Real-Space Observation of Helical Spin Order*, Science **311**, pp.359-361 (2006), https://doi.org/10.1126/science.11206.

[9] S. Mühlbauer, B. Binz, F. Jonietz, C. Pfleiderer, A. Rosch, A. Neubauer, R. Georgii, P. Böni, *Skyrmion Lattice in a Chiral Magnet*, Science, **123**, 915 (2009), https://doi.org/10.1126/science.116676.

[10] X. Yu, Y. Onose, N. Kanazawa, J.H. Park, J.H. Han, Y. Matsui, N. Nagaosa, and Y. Tokura, *Real-space observation of a two-dimensional skyrmion crystal*, Nature **465**, 901-904 (2010), https://doi.org/10.1038/nature09124.

[11] A. N. Bogdanov, and U. K. Röβler, *Chiral Symmetry Breaking in Magnetic Thin Films and Multilayers*, Phys. Rev. Lett., **87**, 037203 (2001), https://doi.org/10.1103/PhysRevLett.87.037203.

[12] A. B. Butenko, A. A. Leonov, U. K. Röβler, and A. N. Bogdanov, *Stabilization of skyrmion textures by uniaxial distortions in noncentrosymmetric cubic helimagnets*, Phys. Rev. B **82**, 052403 (2010), https://doi.org/10.1103/PhysRevB.82.052403.

[13] S. Rohart and A. Thiaville, *Skyrmion confinement in ultrathin film nanostructures in the presence of Dzyaloshinskii-Moriya interaction*, Phys. Rev. B **88**, 184422 (2013), https://doi.org/10.1103/PhysRevB.88.184422.

[14] H. Du, R. Che, L. Kong X. Zhao, C. Jin, C. Wang, J. Yang, W. Ning, R. Li, C. Jin, X. Chen, J. Zang, Y. Zhang, and M. Tian, *Edge-mediated skyrmion chain and its collective dynamics in a confined geometry*, Nature Comm. **6**, 8504 (2015), https://doi.org/10.1038/ncomms9504.

[15] T. Matsumoto, Y.-G. So, Y. Kohno, Y. Ikuhara, and N. Shibata, *Stable Magnetic Skyrmion States at Room Temperature Confined to Corrals of Artificial Surface Pits Fabricated by a Focused Electron Beam*, Nano Lett. 18, 754-762 (2018), https://doi.org/10.1021/acs.nanolett.7b03967.

[16] C. Jin, Zi-An Li, A. Kovács, J. Caron, F. Zheng, F. N. Rybakov, N. S. Kiselev, H. Du, S. Blügel, M. Tian, Y. Z., M. Farle, and Rafal E. Dunin-Borkowski, *Control of morphology and formation of highly geometrically confined magnetic skyrmions*, Nature Comm. **8**, 15569 (2017), https://doi.org/10.1038/ncomms15569.

[17] Z. Hou, Q. Zhang, G. Xu, S. Zhang, C. Gong, B. Ding, H. Li, F. Xu, Y. Yao, E. Liu, G. Wu, X. Zhang, and W. Wa, *Manipulating the Topology of Nanoscale Skyrmion Bubbles by Spatially Geometric Confinement*, ACS Nano. **13**, 922-929 (2019), https://doi.org/10.1021/acsnano.8b09689.

[18] Pin Ho, Anthony K.C. Tan, S. Goolaup, A.L. Gonzalez Oyarce, M. Raju, L.S. Huang, Anjan Soumyanarayanan, and C. Panagopoulos, *Geometrically Tailored Skyrmions at Zero Magnetic Field in Multilayered Nanostructures*, Phys. Rev. Appl. **11**, 024064 (2019), https://doi.org/10.1103/PhysRevApplied.11.024064.

[19] S. Seki, Y. Okamura, K. Shibata, R. Takagi, N. D. Khanh, F. Kagawa, T. Arima, and Y. Tokura, *Stabilization of magnetic skyrmions by uniaxial tensile strain*, Phys.Rev. B **96**, 220404(R) (2017), https://doi.org/10.1103/PhysRevB.96.220404.

[20] Y. Wang, L. Wang, J. Xia, Z. Lai, G. T. X. Zhang, Z. Hou, X. Gao, W. Mi, C. Feng, M. Zeng, G. Zhou, G. Yu, G. Wu, Y. Zhou, W. Wang, X. Zhang, and J. Liu, *Electric-field-driven non-volatile multi-state switching of individual skyrmions in a multiferroic heterostructure*, Nature Comm. **11**, 3577 (2020), https://doi.org/10.1038/s41467-020-17354-7.

[21] H. Li, C. A. Akosa, P. Yan, Y. Wang, and Z. Cheng, *Stabilization of Skyrmions in a Nanodisk Without an External Magnetic Field* , Phys. Rev. Applied. **13**, 034046 (2020), https://doi.org/10.1038/s41467-020-17354-7.

[22] N. Mehmood, J. Wang, C. Zhang, Z. Zeng, J. Wang, and Q. Liu, *Magnetic skyrmion shape manipulation by perpendicular magnetic anisotropy excitation within geometrically confined nanostructures*, J. Mag. Mag. Mat. **545**, 168775 (2022), https://doi.org/10.1016/j.jmmm.2021.168775.

[23] K. Niitsu, Y. Liu, A. C. Booth, X. Yu, N. Mathur, M. J. Stolt, D. Shindo, S. Jin, J. Zang, N. Nagaosa, and Y. Tokura, *Geometrically stabilized skyrmionic vortex in FeGe tetrahedral nanoparticles*, Nature Materials **21**, 305-310 (2022), https://doi.org/10.1038/s41563-021-01186-x.

[24] G. Diguet, B. Ducharne, S. El Hog, F. Kato, H. Koibuchi, T. Uchimoto, and H. T. Diep, *Finsler Geometry Modeling and Monte Carlo Study on Geometrically Confined skyrmions in Nanodot*, Proc. ICFD2023, http://arxiv.org/abs/2308.16199.

[25] R. Friedberg and H.-C. Ren, *Field theory on a computationally constructed random lattice*, Nucl. Phys. B **235**, 310-320 (1984), https://doi.org/10.1016/0550-3213(84)90501-7.

[26] N. Metropolis, A.W. Rosenbluth, M.N. Rosenbluth, A.H. Teller, and E. Teller, *Equation of State Calculations by Fast Computing Machines*, J. Chem. Phys. **21**, 1087 (1953), https://doi.org/10.1063/1.1699114.

[27] D.P. Landau, *Finite-size behavior of the Ising square lattice*, Phys. Rev. B **13**, 2997 (1976), https://doi.org/10.1103/PhysRevB.13.2997.

[28] G. Diguet, B. Ducharne, S. El Hog, F. Kato, H. Koibuchi, T. Uchimoto, and H.T. Diep, *Monte Carlo studies of skyrmion stabilization under geometric confinement and uniaxial strain*, J. Mag. Mag. Mat. **579**, 170819 (2023), https://doi.org/10.1016/j.jmmm.2023.170819.

[29] D. Andrienko, *Introduction to liquid crystals*, J. Mol. Liq., **267**, pp. 520-541 (2018), https://doi.org/10.1016/j.molliq.2018.01.175.

[30] T. Shinjo T. Okuno R. Hassdorf, K. Shigeto and T. Ono, *Magnetic Vortex Core Observation in Circular Dots of Permalloy*, Science **289**, 930 (2000), https://doi.org/10.1126/science.289.5481.930.

[31] T. Okuno, K. Shigeto, T. Ono, K. Mibu and T. Shinjo, *MFM study of magnetic vortex cores in circular permalloy dots: behavior in external field*, J. Mag. Mag. Mat. **240**, pp. 1-6 (2002), https://doi.org/10.1016/S0304-8853(01)00708-9.